

# A sub-micrometer resolution hard X-ray microprobe system of BL8C at Pohang Light Source

Nark-Eon Sung,<sup>a</sup> Ik-Jae Lee,<sup>a\*</sup> Kug-Seong Lee,<sup>a</sup> Seong-Hun Jeong,<sup>a</sup> Seen-Woong Kang<sup>a</sup> and Yong-Bi Shin<sup>b</sup>

<sup>a</sup>Pohang Accelerator Laboratory, Pohang University of Science and Technology, Pohang 790-784, South Korea, and

<sup>b</sup>Gyeongju National Museum, Gyeongju 780-150, South Korea. \*Correspondence e-mail: ijlee@postech.ac.kr

Received 6 February 2015

Accepted 25 July 2015

Edited by S. M. Heald, Argonne National Laboratory, USA

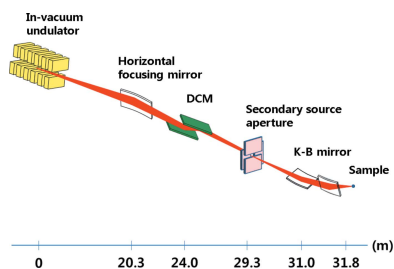
**Keywords:** X-ray instrumentation; microprobe; XAFS; micro-XRF; micro-XANES.

A microprobe system has been installed on the nanoprobe/XAFS beamline (BL8C) at PLS-II, South Korea. Owing to the reproducible switch of the gap of the in-vacuum undulator (IVU), the intense and brilliant hard X-ray beam of an IVU can be used in X-ray fluorescence (XRF) and X-ray absorption fine-structure (XAFS) experiments. For high-spatial-resolution microprobe experiments a Kirkpatrick–Baez mirror system has been used to focus the millimeter-sized X-ray beam to a micrometer-sized beam. The performance of this system was examined by a combination of micro-XRF imaging and micro-XAFS of a beetle wing. These results indicate that the microprobe system of the BL8C can be used to obtain the distributions of trace elements and chemical and structural information of complex materials.

## 1. Introduction

The synchrotron-based microprobe technique combines X-ray fluorescence (XRF), 2D- or 3D-XRF imaging, and X-ray absorption fine-structure (XAFS) techniques, and has been used for non-destructive analysis of trace elements in complex matrices such as organisms, ceramics, minerals and antiques (Takahashi *et al.*, 2006; Karanfil *et al.*, 2012; Somogyi *et al.*, 2005). Although the spatial resolution of the microprobe technique is not better than the other micro-analytical techniques such as transmission electron microscopy and scanning electron microscopy, the microprobe technique has several advantages such as non-destructiveness, long penetration depth, high sensitivity and energy tunability (Majumdar *et al.*, 2012). For microprobe experiments with high spectral resolution, an intense and brilliant X-ray source is essential. An undulator is a kind of synchrotron-radiation source; it is suitable for microprobe experiments due to its high brilliance and narrow spectral range (Chapman *et al.*, 1989; Kim, 1986; Attwood *et al.*, 1985; Boyanov *et al.*, 1994).

XRF uses energy-dispersive detectors to provide information on elemental concentrations at a spot and on elemental distributions over a specified area at appropriate excitation energy. In contrast, XAFS provides chemical and structural information around X-ray absorbing atoms at the spot (Bichlmeier *et al.*, 2001; Adams *et al.*, 1998; Majumdar *et al.*, 2012; Fittschen & Falkenberg, 2011). Owing to the energy tunability of the synchrotron radiation, XRF experiments can be conducted alternatively with XAFS (Majumdar *et al.*, 2012; Tancharakorn *et al.*, 2012). XRF can be extended to XRF tomography by obtaining two-dimensional elemental distribution images at different angles. Probing of a small spot or area of interest requires a well focused X-ray beam, smaller than or equal to the spot size. X-ray focusing optics such



© 2015 International Union of Crystallography

as tapered capillary X-ray lenses, zone-plates, compound refractive lenses and Kirkpatrick–Baez (K–B) mirrors have been used to produce a micrometer-sized or submicrometer-sized beam (Ice *et al.*, 2000; Yang *et al.*, 1995; Howells *et al.*, 2000; Snigirev *et al.*, 1996; Kirkpatrick & Baez, 1948; Yang, 1993; Lengeler *et al.*, 1999). As a result of advances in X-ray focusing optics, beams with a diameter of a few tens of nanometers have been realised (Majumdar *et al.*, 2012; Liu *et al.*, 2005; Matsuyama *et al.*, 2006). However, achieving nanometer resolution is still a major challenge. Depending on the purpose and required resolution of experiments, appropriate focusing optic devices can be used.

A helium-filled K–B mirror system (JTEC, Japan) has been installed at the 8C nanoprobe/XAFS beamline (BL8C) at the Pohang Light Source (PLS-II) for use in probing micro-scale regions. To minimize the mechanical vibration for microprobe experiments, the K–B mirror system, including optical zoom lens and precision positioning system, is mounted on a heavy granite table. This paper describes the performance of the beamline and its capabilities with examples of measured results.

## 2. Beamline overview

### 2.1. Beamline and radiation source

The specifications of the BL8C and in-vacuum undulator (IVU) are tabulated in Tables 1 and 2. PLS-II operates at 3.0 GeV and  $\geq 300$  mA in top-up injection mode. The in-vacuum undulator (IVU) (Table 2) is a hybrid- and asymmetric-type; it is 1.4 m long with 20 mm period and 140 poles. The gap range of the IVU is 5.1–20.0 mm with a maximum taper of 1.2 mm. The beam size at source point is  $12 \mu\text{m} \times 187 \mu\text{m}$  (V  $\times$  H) and the beam divergence is  $12 \mu\text{rad} \times 49 \mu\text{rad}$  (V  $\times$  H). The available X-ray energy range of the BL8C is 4.0–22.0 keV.

At BL8C (Fig. 1), a rhodium-coated (30 nm-thick) horizontal focusing mirror (HFM) and a double-crystal monochromator (DCM) with Si(111) crystals are placed at 20.3 m

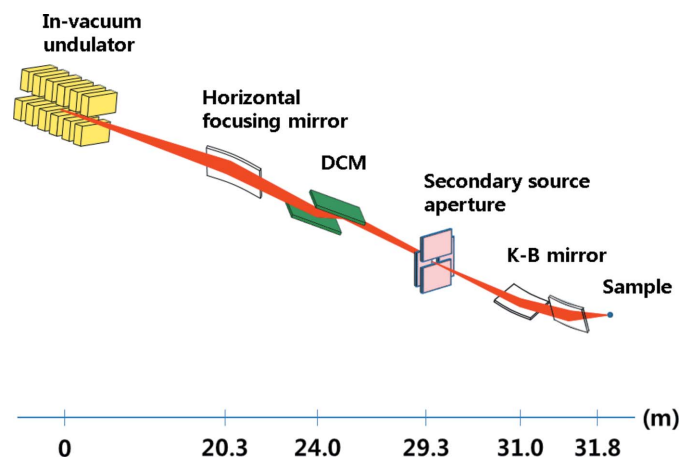


**Figure 1**  
Schematic layout of the nanoprobe/XAFS beamline (BL8C). Positions of important optical components from the source point are shown.

**Table 1**  
Specifications of BL8C.

Name of the beamline	Nanoprobe/XAFS
Port	8C
Source type	In-vacuum undulator, hybrid, asymmetric
Energy range	4.0–22.0 keV
Energy resolution ( $\Delta E/E$ )	$< 2 \times 10^{-4}$
Photon flux (at 5.4 keV)	$\sim 1 \times 10^{12}$ photons $\text{s}^{-1}$
Beam size at sample	$\sim 0.5 \mu\text{m} \times 0.5 \mu\text{m}$ (V $\times$ H) by K–B mirror
DCM	Si(111)
Experimental techniques	( $\mu$ -)XRF, ( $\mu$ -)XAFS

**Table 2**  
Specifications of the in-vacuum undulator of BL8C.

Source type	In-vacuum undulator, hybrid, asymmetric
Magnet block material	$\text{Sm}_2\text{Co}_{17}$
Period length	20 mm
Period number	70
Undulator length	1400 mm
Working gap range	5–20 mm
Source beam size	$12 \mu\text{m} \times 200 \mu\text{m}$ (V $\times$ H)
Beam divergence	$10 \mu\text{rad} \times 47 \mu\text{rad}$ (V $\times$ H)

and 24.0 m from the radiation source, respectively. To alleviate the thermal load problem, all optical components are cooled by water except the DCM, which is cooled by liquid nitrogen. The synchrotron radiation from the IVU is collimated by apertures and focused horizontally by the HFM, which also reduces horizontal perturbation of synchrotron-radiation and contamination by high-order harmonics. The HFM is designed to have a focal point at the secondary source aperture (SSA) position, 29.3 m from the radiation source. X-rays are monochromated by the DCM and delivered to the SSA. The SSA is used to define precisely the size of the outgoing X-ray beam which is refocused by subsequent focusing devices. The beamline includes several other components such as masks, apertures, beam monitoring screens and slits. The combination of the apertures and slits allows shaping of the X-ray beam dimensions and removal of parasitic waves. The X-ray beam is delivered to the K–B mirror system directly from the SSA through a vacuum pipe and can be focused to sub-micrometer resolution.

### 2.2. Microprobe setup

The K–B focusing optics (Table 3) consists of a pair of tangential-ellipse-shaped silicon crystals that focus the incident X-rays vertically and horizontally in sequence with fixed curvatures. The vertical mirror is 300 mm long and has a focal length of 474 mm; the horizontal mirror is 200 mm long and has a focal length of 214 mm. Both mirrors have 7 mm-wide bare silicon, platinum- and rhodium-coated stripes (60 nm thick). The incident angles of X-rays of both mirrors are 3.0 mrad. Both mirrors have a roughness of  $< 0.14$  nm. The tangential and sagittal slope errors of both mirrors were measured using a surface profiler (MSI and RADSI, Jigyo, Japan) and were  $< 0.19$  and  $< 0.14 \mu\text{rad}$ , respectively.

The K–B mirrors are aligned to the X-ray direction using a motor-driven seven-axis mount and a manual six-axis K–B mirror manipulator. A dual-magnification  $7\times$  optical zoom

Table 3

Optical parameters of the K–B focusing mirrors (all parameters were measured using the MSI and RADSI surface profiler instrument).

	Vertical focusing mirror	Horizontal focusing mirror
Surface shape	Tangential-ellipse	Tangential-ellipse
Mirror length (mm)	300	200
Mirror width (mm)	50.0	50.0
Substrate material	Si	Si
Surface coating	Rh, Pt, Si	Rh, Pt, Si
Width of coating (mm)	7	7
Coating thickness (nm)	58	58
Incident angle (mrad)	3.0	3.0
Focal length (mm)	474	214
Surface roughness (nm)	0.13	0.12
Tangential slope error ( $\mu\text{rad}$ )	0.19	0.13
Sagittal slope error ( $\mu\text{rad}$ )	0.14	0.11
Demagnification factor	65.9	10.5

lens system (Optem, USA) mounted on a motorized XYZ stage (Aerotech, USA) was installed around the focal point of the K–B mirrors to monitor the sample state. Motor precisions of the lens-stage are  $0.2\ \mu\text{m}$ . X-ray position and selected sample area around the focal point are monitored by CCD cameras that are connected to a computer monitor and mounted on the optical zoom lenses. The focal length of the zoom lens can be adjusted using the lens stage, or a built-in motor on the body tube of the zoom lens. Depending on the required optical field of view, the magnification of the system can be changed by replacing the objective lens or by adjusting a motor-driven zoom lens. The sample position can be adjusted using a three-axis sample stage (Aerotech, USA) that has a resolution of  $\geq 1\ \text{nm}$ . The microprobe experimental system (Fig. 2) in the hutch of the BL8C is composed of a K–B mirror system, sample stages, a lens stage, a video zoom microscope and detectors. An energy-dispersive seven-element low-energy Ge array detector (LEGe, Canberra, USA) is used for XRF experiments.

We developed software which is used to find the beam position and to set the 2D region of interest using the zoom lens stage, and to set the sample stage through a graphical user interface. This software also obtains raster-scanned 2D XRF images and XAFS spectra by controlling the sample stage. To achieve a submicrometer X-ray beam at the sample position, the K–B mirror system was designed to have large demagnification factors [69.7 (V), 10.5 (H)]. Because the focal point of the HFM is at the SSA position, the horizontal size of the focused beam by the K–B mirror system depends on the horizontal width of the SSA. However, the vertical beam size of the focused beam is relatively insensitive to the vertical aperture width of the SSA.

### 2.3. Profiles of the focused beam

Horizontal and vertical beam profiles (Fig. 3) of the focused beam at the focal point of the K–B mirrors were obtained by the conventional knife-edge method using a gold wire of diameter  $200\ \mu\text{m}$ . The gold wire was placed on the sample stage at the focal points of the K–B mirror system, and was

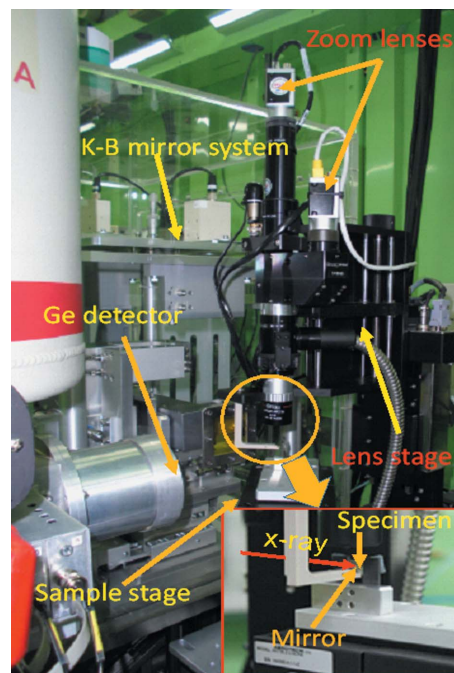


Figure 2 Pictorial view around the sample position. The microprobe experimental system is composed of a K–B mirror system, sample stages, video zoom microscope and detectors. A low-energy Ge array detector is used for fluorescence measurements.

scanned across the focused beam in steps of  $\leq 0.1\ \mu\text{m}$ . The beam profiles were obtained by measuring the underscreened X-ray intensities from the gold wire using a nitrogen gas-filled ionization chamber (IC), placed downstream of the gold wire. The theoretical size of the vertical beam is  $\sim 0.5\ \mu\text{m}$  when the vertical width of the SSA is opened to  $\geq 0.5\ \text{mm}$ . The theoretical size of the horizontal beam is similar to that of the vertical beam when the horizontal width of the SSA is  $0.01\ \text{mm}$ . Thus, the aperture width of the SSA was set to  $0.5\ \text{mm} \times 0.01\ \text{mm}$  (V  $\times$  H) to achieve a rectangular minimum

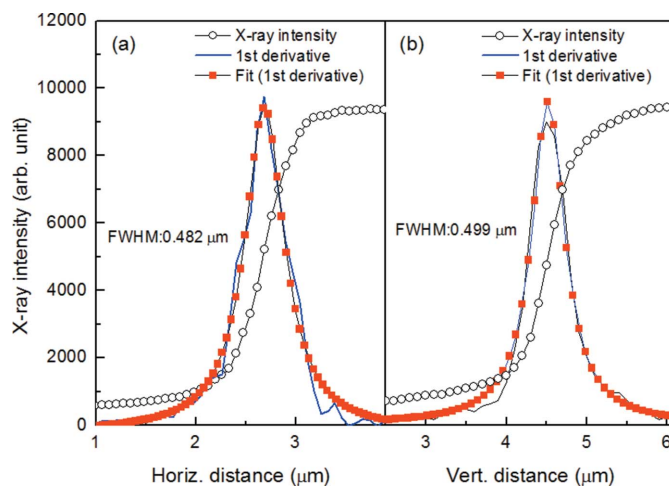


Figure 3 (a) Horizontal and (b) vertical beam profiles of the focused beam at the focal point of the K–B mirrors. The beam profiles were obtained by the conventional knife-edge method using a gold wire of diameter  $200\ \mu\text{m}$ .

beam size. The first derivatives of the beam profiles were fitted using a Lorentz function. The full width at half-maximum of the horizontal and vertical beam profile was  $\sim 0.5 \mu\text{m}$ ; these results closely match the designed values of the K–B mirror system. The resulting spot size at the focal plane of about  $0.499 \mu\text{m} \times 0.482 \mu\text{m}$  (V  $\times$  H) is shown in Fig. 3.

### 3. Experimental techniques available at BL8C

#### 3.1. Micro-XRF imaging

XRF is a powerful ‘non-destructive’ technique for the elemental analysis of materials at the micro and trace level. This technique finds several applications in a variety of fields such as geology, archaeology, biomedical science and material science, *etc.* XRF analysis in BL8C enables multi-element mapping and quantitative analysis (down to the sub-p.p.m. level) with a micrometer- or submicrometer-sized beam. The spatial resolution and capability of the  $\mu$ -XRF mapping were examined by measuring the fluorescence X-rays from a selected area of a test pattern (X50-30-2, Xradia, USA) (Fig. 4). The test pattern was mounted on the sample stage at the focal point of the K–B mirror system and raster-scanned in  $0.6 \mu\text{m}$  steps in both horizontal and vertical directions. To normalize the fluorescence intensity, the incident X-ray intensities were monitored using a nitrogen gas-filled IC. 2D-XRF images were obtained by measuring Au  $L_{\alpha}$  fluorescence lines using the LEGe detector with an excitation energy of 13.5 keV. XRF spectra were measured at each point for 0.5 s. The XRF images show that the microprobe system of the BL8C has sufficient spatial resolution to resolve a spot of  $\leq 1 \mu\text{m}^2$ .

The trace-elements distribution of a beetle wing (*Buprestis haemorrhoidalis*) was obtained by measuring fluorescence lines of transition elements using the LEGe detector with an excitation energy of 13.5 keV (Fig. 5). The beetle wing was cut by sawing machine to have long cross section, immersed in resin and polished. It was raster-scanned in  $5 \mu\text{m}$  steps in both horizontal and vertical directions covering an area of  $182 \mu\text{m} \times 1070 \mu\text{m}$  (V  $\times$  H) with an integration time of 0.3 s at each point. XRF images show that some elements are concentrated in a small region or dispersed with low concentration. To show the distribution of trace elements regardless of concentrations, XRF images were not normalized. It is

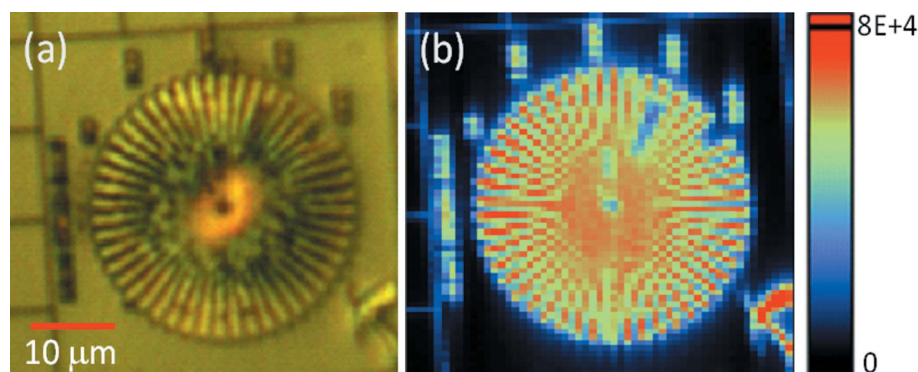


Figure 4

(a) Optical image of a test pattern (Siemens star). (b) 2D-XRF image obtained by measuring Au  $L_{\alpha}$  fluorescence lines using the LEGe detector. It was measured using a  $0.6 \mu\text{m}$  (V)  $\times$   $0.6 \mu\text{m}$  (H) focused beam with  $0.6 \mu\text{m}$  steps.

observed that more Fe and Zn is distributed in the beetle wing in comparison with other elements.

#### 3.2. Micro-XAFS experiments

The XAFS technique includes XANES and extended X-ray absorption fine-structure (EXAFS). EXAFS is used to analyze the local structure around an X-ray absorbing atom, whereas XANES gives the chemical information owing to its elemental specificity by sweeping the energy around the absorption edge of an X-ray absorbing atom. Currently, BL8C has achieved a beam size down to  $0.5 \mu\text{m}$  using the K–B mirror for the  $\mu$ -XAFS measurement, which paves the way for a new level of experimental analysis of the heterogeneous samples or individual nanostructures in biological, environmental and mate-

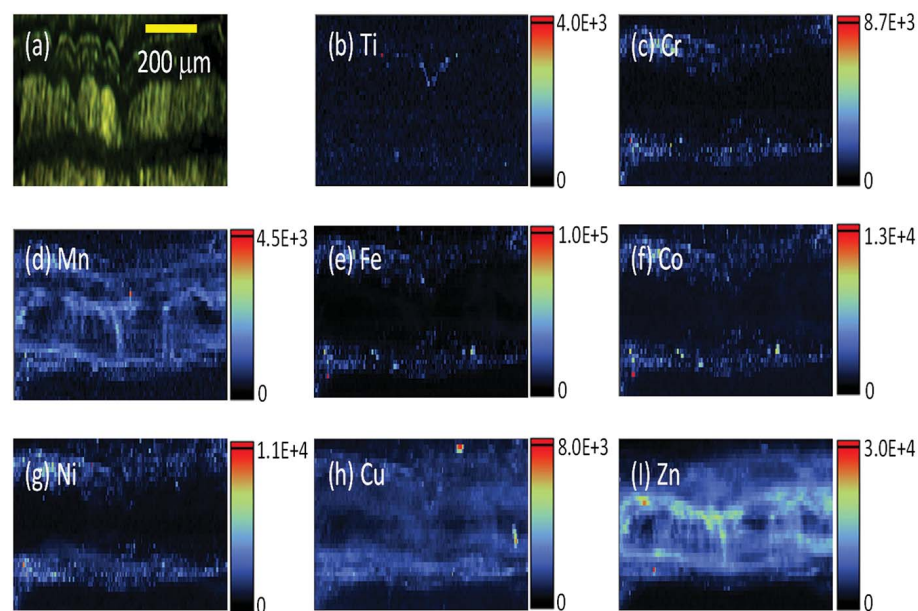


Figure 5

(a) Optical image of a part of the beetle wing. (b)–(i) Distribution maps of trace elements included in the beetle wing. To show the distribution of trace elements regardless of concentration, XRF images were not normalized. XRF images were measured using a  $5 \mu\text{m}$  (V)  $\times$   $5 \mu\text{m}$  (H) focused beam with  $5 \mu\text{m}$  steps.

rials science. At BL8C, the photon energy range of 4–22 keV will cover *K*- or *L*-absorption edges of most elements and the  $\mu$ -XANES measurement can be performed either in transmission or in fluorescence mode.

The performance of the microprobe system of BL8C was examined by measuring XAFS spectra of a beetle wing. Preliminary scanned Fe and Zn *K*-edge XAFS spectra of the beetle wing at several points showed nearly the same spectral features. Thus, Fe *K*-edge  $\mu$ -XAFS spectra were measured at point 1 (Fig. 6a) where the concentration of Fe is higher than other points as was shown in Fig. 5(a). In comparison with  $\mu$ -XANES spectra of the Fe reference materials (Fig. 6b), chemical and electronic states of Fe of point 1 are different from those of the reference materials. The Fe *K*-edge EXAFS oscillation and Fourier-transformed (FT) magnitudes are shown in Figs. 6(c)–6(d). The available energy range for the FT is 2.5–11.0  $\text{\AA}^{-1}$ . Due to the dilution of Fe in the beetle wing, the scanning time was longer than four times that of the reference materials. The local structure of Fe is not matched to

those of the reference materials. Zn *K*-edge  $\mu$ -XAFS spectra of point 2 in the beetle wing (Fig. 7) show that the oxidation state of Zn in the beetle wing is around 2+, but the spectral feature is different from that of the ZnO. The scanning time for the beetle wing was longer than three times that of the reference materials. The EXAFS oscillation and FT magnitudes of the Zn *K*-edge are shown with those of the reference materials [Figs. 7(b)–7(d)]. The Fourier transformation was performed with an available energy range of 2.5–9.5  $\text{\AA}^{-1}$ .

#### 4. Facility access

Beam times of the BL8C are distributed to the general users through a website (<http://pal.postech.ac.kr>) which accepts proposals (three terms per year and peer-review by committee) with three different access programs: (i) regular proposals, (ii) long-term proposals and (iii) urgent request proposals which can be submitted any time but the allocation of beam time depends on its urgency and importance. In

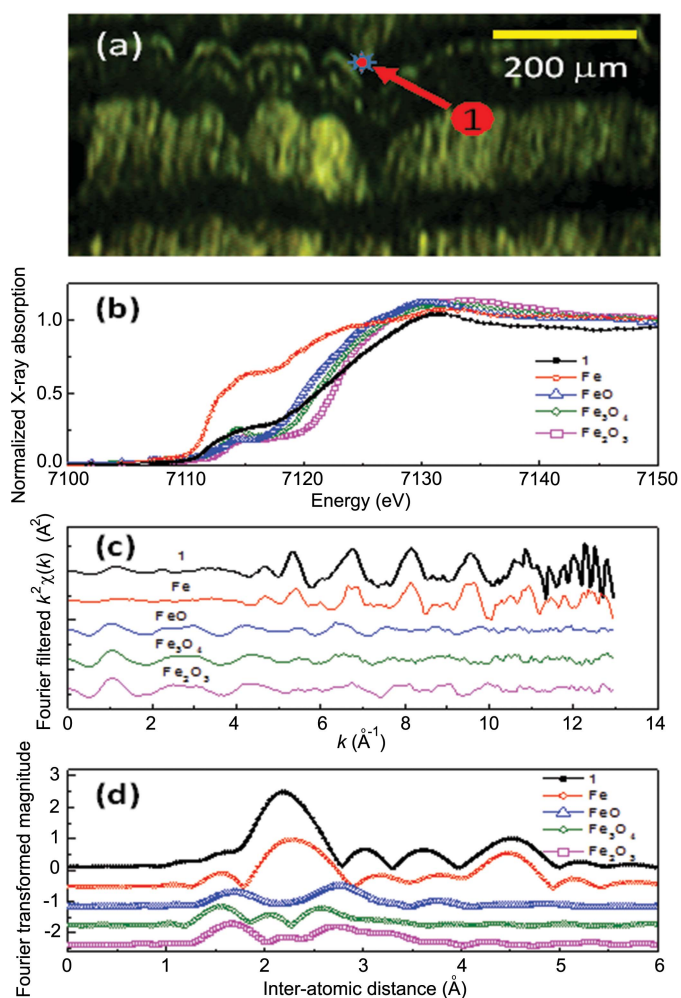


**Figure 6** (a) Optical image of part of the beetle wing. Point 1, where the concentration of Fe is higher than other parts, was chosen for the Fe *K*-edge XAFS. (b)–(d) Fe *K*-edge  $\mu$ -XANES spectra, EXAFS oscillation and FT magnitudes of the reference materials and beetle wing, respectively.

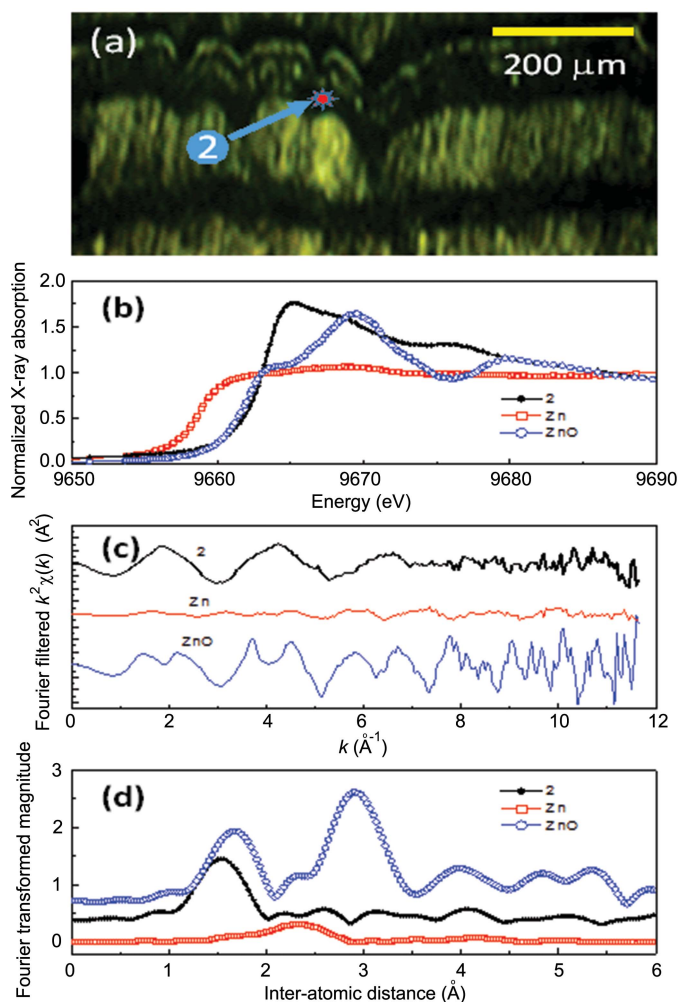


**Figure 7** (a) Optical image of part of the beetle wing. Zn *K*-edge XAFS were obtained at point 2 where the concentration of Zn is higher than at other points. (b)–(d) Zn *K*-edge  $\mu$ -XANES spectra, EXAFS oscillation and FT magnitudes of the reference materials and beetle wing, respectively.

general, 70% of beam time is devoted to general users, and the rest is reserved to beamline staff for beamline upgrading and developing experimental techniques. For efficient user service, beam time is classified into two: (i) general XAFS experiments, (ii) microprobe and micro-XAFS experiments. The beam time portion of the microprobe/XAFS depends on the number of proposals for the microprobe/XAFS.

## 5. Summary and conclusions

A microprobe system that uses a K–B mirror system for final beam focusing has been installed in BL8C at PLS-II, South Korea. Because the IVU provides intense and brilliant synchrotron radiation, BL8C is suitable for use as a high-spectral-resolution microprobe. The HFM, DCM and apertures are located in front of the K–B mirror system to focus, collimate and monochromatize the X-ray beam. The beam size after focusing by the K–B mirror system was as small as 0.5  $\mu\text{m}$ .

The XRF image of an Au pattern shows that the spatial resolution of the microprobe system is finer than 1  $\mu\text{m}$ . Micro-XRF imaging,  $\mu$ -XANES and  $\mu$ -EXAFS techniques were combined to probe the oxidation states and structural information of a part of a beetle wing. A  $\mu$ -XRF image of the beetle wing shows that Zn is distributed evenly with relative high concentration, but Fe is localized with high concentration. Fe and Zn K-edge XAFS spectra of the beetle wing were measured at specific points to examine the performance of BL8C.

The results of  $\mu$ -XRF imaging and  $\mu$ -XAFS indicate that the microprobe system of the BL8C has a high spatial resolution, and therefore can be applicable to analyze the distributions of trace elements and to obtain chemical and structural information of complex materials.

## Acknowledgements

The microprobe experiments were performed with approval of authorities from the PLS-II, South Korea. This research was supported by the Basic Science Research Program through the National Research Foundation of Korea (NRF) funded by

the Ministry of Education, Science and Technology (2011-0022268).

## References

- Adams, F., Janssens, K. & Snigirv, A. (1998). *J. Anal. Atom. Spectrom.* **13**, 318.
- Attwood, D., Halbach, K. & Kim, K.-J. (1985). *Science*, **228**, 1265–1272.
- Bichlmeier, S., Janssens, K., Heckel, J., Gibson, D., Hoffmann, P. & Ortner, H. M. (2001). *X-ray Spectrom.* **30**, 8–14.
- Boyanov, B. I., Bunker, G., Lee, J. M. & Morrison, T. I. (1994). *Nucl. Instrum. Methods Phys. Res. A*, **339**, 596–603.
- Chapman, K., Lai, B., Cerrina, F. & Viccaro, J. (1989). *Nucl. Instrum. Methods Phys. Res. A*, **283**, 88–99.
- Fittschen, U. E. A. & Falkenberg, G. (2011). *At. Spectrosc.* **66**, 567–580.
- Howells, M. R., Cambie, D., Duarte, R. M., Irick, S., MacDowell, A. A., Padmore, H. A., Renner, T. R., Rah, S. & Sandler, R. (2000). *Opt. Eng.* **39**, 2748–2762.
- Ice, G. E., Chung, J. S., Tischler, J. Z., Lunt, A. & Assoufid, L. (2000). *Rev. Sci. Instrum.* **71**, 2635–2639.
- Karanfil, C., Bunker, G., Newville, M., Segre, C. U. & Chapman, D. (2012). *J. Synchrotron Rad.* **19**, 375–380.
- Kim, K.-J. (1986). *Nucl. Instrum. Methods Phys. Res. A*, **246**, 67–70.
- Kirkpatrick, P. & Baez, A. V. (1948). *J. Opt. Soc. Am.* **38**, 766–774.
- Lengeler, B., Schroer, C. G., Richwin, M., Tümmeler, J., Drakopoulos, M., Snigirev, A. & Snigireva, I. (1999). *Appl. Phys. Lett.* **74**, 3924–3926.
- Liu, W., Ice, G. E., Tischler, J. Z., Khounsary, A., Liu, C., Assoufid, L. & Macrander, A. T. (2005). *Rev. Sci. Instrum.* **76**, 113701.
- Majumdar, S., Peralta-Videa, J. R., Castillo-Michel, H., Hong, J., Rico, C. M. & Gardea-Torresdey, J. L. (2012). *Anal. Chim. Acta*, **755**, 1–16.
- Matsuyama, S., Mimura, H., Yumoto, H., Sano, Y., Yamamura, K., Yabashi, M., Nishino, Y., Tamasaku, K., Ishikawa, T. & Yamauchi, K. (2006). *Rev. Sci. Instrum.* **77**, 103102.
- Snigirev, A., Kohn, V., Snigireva, I. & Lengeler, B. (1996). *Nature (London)*, **384**, 49–51.
- Somogyi, A., Tucoulou, R., Martinez-Criado, G., Homs, A., Cauzid, J., Bleuet, P., Bohic, S. & Simionovici, A. (2005). *J. Synchrotron Rad.* **12**, 208–215.
- Takahashi, Y., Uruga, T., Tanida, H., Terada, Y., Nakai, S. & Shimizu, H. (2006). *Anal. Chim. Acta*, **558**, 332–336.
- Tancharakorn, S., Tanthanuch, W., Kamonsutthipajit, N., Wongprachanukul, N., Sophon, M., Chaichuay, S., Uthaisar, C. & Yimmirun, R. (2012). *J. Synchrotron Rad.* **19**, 536–540.
- Yang, B. X. (1993). *Nucl. Instrum. Methods Phys. Res. A*, **328**, 578–587.
- Yang, B. X., Rivers, M., Schildkamp, W. & Eng, P. J. (1995). *Rev. Sci. Instrum.* **66**, 2278–2280.